Single-crystal Pt-decorated WO_3 ultrathin films: a platform for sub-ppm hydrogen sensing at room temperature

Mattoni, Giordano; de Jong, Bas; Manca, Nicola; Tomellini, M.; Caviglia, Andrea

DOI
10.1021/acsanm.8b00627

Publication date
2018

Document Version
Final published version

Published in
ACS Applied Nano Materials

ACS APPLIED NANO MATERIALS

Article

Cite This: ACS Appl. Nano Mater. 2018, 1, 3446−3452

www.acsanm.org

Single-Crystal Pt-Decorated WO_3 Ultrathin Films: A Platform for Sub-ppm Hydrogen Sensing at Room Temperature

Giordano Mattoni,*[,†] Bas de Jong,[†] Nicola Manca,[†] Massimo Tomellini,[‡] and Andrea D. Caviglia[†]

[†]Kavli Institute of Nanoscience, Delft University of Technology, 2628 CJ Delft, The Netherlands

[‡]Dipartimento di Scienze e Tecnologie Chimiche, Università di Roma Tor Vergata, via della Ricerca Scientifica 1, 00133 Roma, Italy

Supporting Information

ABSTRACT: Hydrogen-related technologies are rapidly developing, driven by the necessity of efficient and high-density energy storage. This poses new challenges to the detection of dangerous gases, in particular the realization of cheap, sensitive, and fast hydrogen sensors. Several materials are being studied for this application, but most present critical bottlenecks, such as high operational temperature, low sensitivity, slow response time, and/or complex fabrication procedures. Here, we demonstrate that WO_3 in the form of single-crystal, ultrathin films with a Pt catalyst allows high-performance sensing of H_2 gas at room temperature. Thanks to the high electrical resistance in the pristine state, this material is able to detect hydrogen concentrations down to 1 ppm near room temperature. Moreover, the high surface-to-volume ratio of WO_3 ultrathin films determines fast sensor response and recovery, with characteristic times as low as 1 s when the concentration exceeds 100 ppm. By modeling the hydrogen (de)intercalation dynamics with a kinetic model, we extract the energy barriers of the relevant processes and relate the doping mechanism to the formation of oxygen vacancies. Our results reveal the potential of single-crystal WO_3 ultrathin films toward the development of sub-ppm hydrogen detectors working at room temperature.

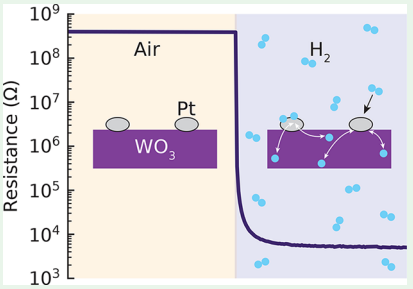

KEYWORDS: *hydrogen sensing, ultrathin films, room temperature gas detection, WO_3 single crystals, kinetics of intercalation and deintercalation*

INTRODUCTION

Transition metal oxides are a class of materials whose properties can be tuned by several external parameters, such as heteroepitaxial strain,[1] electrostatic doping,[2,3] intercalation of other species,[4] or oxygen vacancies.[5−7] This versatility recently triggered a broad technological interest, which goes from their use in oxide-based fuel cells,[8,9] memristive systems,[10−12] neuromorphic architectures,[13,14] chemical actuators,[15] and gas sensors.[16] In this framework, oxide compounds are of particular interest for building high-performance hydrogen sensors, motivated by the growing demand for using H_2 gas to transport and store energy and to reduce the safety risks imposed by this explosive gas.[17,18] Several oxide materials have been employed for resistive hydrogen sensing, with TiO_2, SnO_2, VO_2, and WO_3 being among the most prominent ones.[19−22] WO_3, in particular, is regarded as a very promising candidate because incorporation of hydrogen changes its electrical resistance by several orders of magnitude.[23,24] As summarized in Table 1, hydrogen sensing has been demonstrated with various forms of WO_3, such as amorphous layers and nanostructured materials.[25−30] These sensors, however, usually require a high operational temperature, resulting in high power consumption and poor long-term stability, and have a sensitivity limited to hydrogen concentrations of hundreds of ppm.

In this work, we show that single-crystal WO_3 ultrathin films with a Pt catalyst can detect H_2 concentrations down to 1 ppm, with a fast response time, while working at or nearby room temperature. We show that hydrogen intercalation in the WO_3 crystal lattice determines changes of more than 5 orders of magnitude in the electrical resistivity of the material and that

Table 1. Comparison of WO_3-Based Technologies for H_2 Sensing

technology	operational temp (°C)	lower detection limit (ppm)	response time τ (s)
electrodeposited 200 nm films[26]	25	50000	42 (at 25 °C, 50000 ppm)
sputtered 160 nm films[25]	30−300	1250	−
nanoplates[30]	25	1000	24 (at 25 °C, 1000 ppm)
nanowires[28]	30−250	100	300 (at 250 °C, 1000 ppm)
nanocomposites[29]	180−240	50	26 (at 240 °C, 200 ppm)
nanodots[27]	25−350	20	100 (at 150 °C, 1000 ppm)
single-crystal 9 nm ultrathin films (this work)	25−65	1	1 (at 65 °C, 100 ppm)

Received: April 17, 2018
Accepted: June 19, 2018
Published: June 20, 2018

DOI: 10.1021/acsanm.8b00627
ACS Appl. Nano Mater. 2018, 1, 3446−3452

this fully reversible process is mediated by a small amount of platinum catalyst. Response time and lower detection limit can be tuned by temperature, which are reduced by an order of magnitude at a slightly elevated temperature of 65 °C. We study the hydrogen dynamics by modeling the intercalation and deintercalation processes with a series of coupled kinetic equations and extract the characteristic energy scales related to H_2 dissociation, incorporation, and recombination phenomena. We also demonstrate that hydrogen doping is a powerful control parameter to modulate the physical state of WO_3, which can be stabilized in kinetically arrested configurations just below room temperature. Our results show that single-crystal WO_3 ultrathin films are strong candidates for next-generation hydrogen sensing devices, combining high sensitivity, fast response, and device scalability.

RESULTS AND DISCUSSION

WO_3 Material Preparation. We grow a 24 unit cell (uc) crystalline WO_3 film on a $SrTiO_3$ (001) substrate by pulsed laser deposition (growth details in the Experimental Section and ref 31). The WO_3 structural properties are investigated by X-ray diffraction (XRD) and presented in Figure 1a, where finite size oscillations indicate high crystalline quality and confirm the expected film thickness of 9 nm. The reciprocal space map in Figure 1b shows that the material is a single crystal, coherently oriented to the substrate lattice. Surface topography, investigated by atomic force microscopy (AFM) in Figure 1c, shows a step and terrace structure which mimics the underlying substrate morphology. The hydrogen reaction is made possible by the presence of a catalyst, whose function is to facilitate the splitting of H_2 molecules from gas phase into atomic hydrogen, which is absorbed into the WO_3 lattice. In this work, we use platinum, which has the advantage of a high catalytic efficiency together with a low reactivity with oxide materials.[32,33] A Pt layer having nominal thickness of 1 nm is deposited at room temperature by evaporation in vacuum (Figure 1d). Deposition of this low amount of material is expected to form sparse droplets of a few nanometers, and their catalytic activity is confirmed by the data discussed in the following section. Electrical measurements are performed on 50 μm × 50 μm patterned squares measured in van der Pauw configuration, as shown in the optical image of Figure 1e (details in the Experimental Section). The experimental setup is sketched in Figure 1f. We mount the sample in a vacuum chamber (base pressure $p < 1 \times 10^{-4}$ mbar), which is placed in a dark environment. Mixtures of H_2 in Ar carrying gas, with concentration C_{H_2} ranging from 20% down to 1 ppm, are prepared in a series of preparation chambers before exposing the sample. The system also allows to regulate the total pressure of the gas mixture from 1 bar down to 1 mbar.

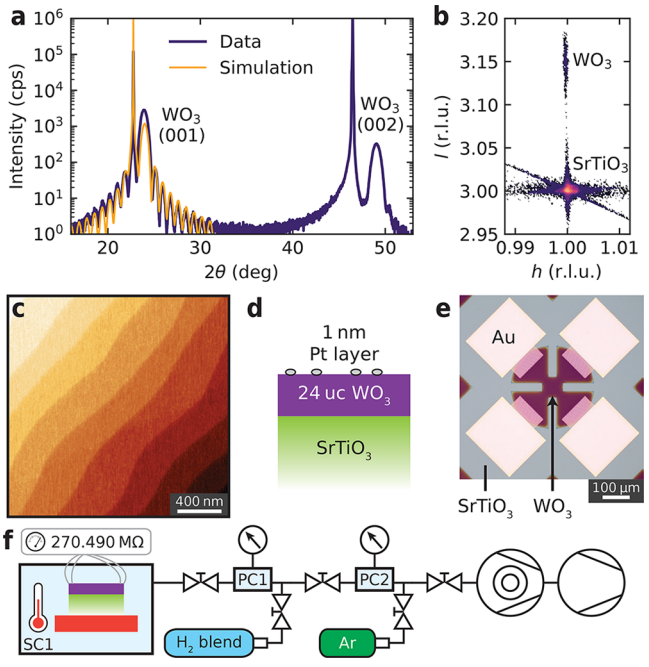

Figure 1. Characterization and preparation of WO_3 thin films. (a) θ–2θ X-ray diffraction scan showing the (001) and (002) peaks of the WO_3 thin film with finite size oscillations around the sharp peaks of the $SrTiO_3$ substrate. (b) Reciprocal space map around the (103) peak. (c) Atomic force microscopy of the WO_3 surface. (d) Schematic of the $WO_3/SrTiO_3$ heterostructure after the evaporation of the Pt catalyst. (e) Optical image of the WO_3 sample patterned in van der Pauw geometry (the image is taken before the removal of the resist for better contrast). (f) Schematic of the experimental setup comprising the sample anchored on a Peltier element (red), the vacuum chamber SC1, the four-probe configuration used for resistive readout, the series of preparation chambers (PC1, PC2), gas bottles, pressure sensors, and vacuum pumps used to prepare the gas mixture (details in the Experimental Section).

WO_3 Response to Hydrogen. The high crystal quality of the WO_3 material determines a high electrical resistance of the pristine device R = 400 MΩ at room temperature. This corresponds to a resistivity of 360 Ω cm, consistent with previous reports of high quality WO_3 thin films with negligible amount of oxygen vacancies.[31] In Figure 2 we show that upon exposure to a high hydrogen concentration (C_{H_2} = 5%, 1 bar total pressure) at room temperature the resistance drops by 5 orders of magnitude, and after a few minutes it saturates to a constant value. When the sample chamber is evacuated, the resistance stays approximately constant, indicating that the doped state is stable over time. When the doped device is exposed to air, the electrical resistance increases over time, recovering more than 3 orders of magnitude in the first 10 min and reaching the initial state after several hours.

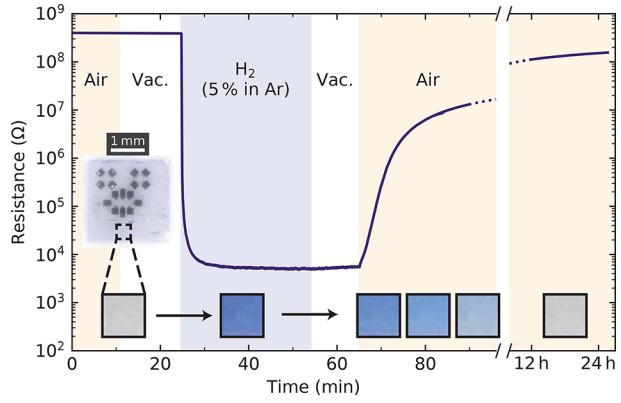

Figure 2. Room temperature electrical and optical changes with hydrogen gas. The WO_3 thin film is exposed to different environmental conditions: 1 bar of air, 1 bar of hydrogen mixture, and vacuum. Both electrical resistance and sample color (optical images) change upon exposure to H_2 and recover their initial state once in air (see also the video in the Supporting Information).

DOI: 10.1021/acsanm.8b00627
ACS Appl. Nano Mater. 2018, 1, 3446−3452

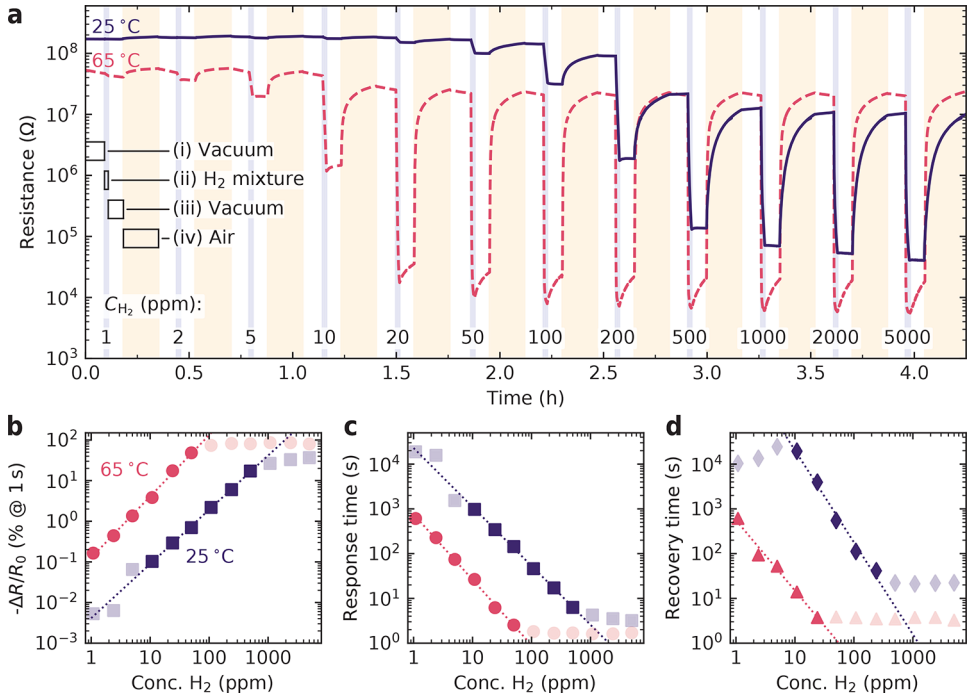

Figure 3. Resistive sensing of different hydrogen concentrations. (a) Resistance variation upon 1 min of exposure to different concentrations of H_2 gas in Ar (1 bar total pressure). The experimental steps consist of (i) sample chamber evacuation ($p < 1 \times 10^{-4}$ mbar), (ii) exposure to the H_2/Ar mixture for 1 min, (iii) chamber evacuation, and (iv) exposure to air for 10 min. The curves are measured at a sample temperature of 25 °C (solid blue) and 65 °C (dashed red). (b) Percentage resistive variation at 1 s after exposure to H_2 and (c) corresponding response time. (d) Recovery time upon exposure to air. The dotted lines are linear fits to the solid markers, while the grayed-out data points are either below the sensor detection limit (low ppm) or in its saturation regime (high ppm).

During the electrical measurement, we took a series of photographs of an unpatterned WO_3 region which is presented in Figure 2 at the corresponding time. The material color changes, switching to blue upon the introduction of the gas (doped state), and going back to the initial transparency when the resistance progressively recovers its original value (see also the video in the Supporting Information). This color change is a well-known effect of hydrogen doping of WO_3, consistent with previous reports.[26,34,35] Both the resistance and optical data indicate that the measured changes in the sample properties are due to hydrogen intercalation and deintercalation into the WO_3 lattice.[36] Moreover, the data show that hydrogen doping is a reversible process and that the deintercalation is facilitated by the presence of air.

Although a precise description of the doping mechanism is still a matter of debate, several reports show that the incorporation of atomic hydrogen determines electron doping of WO_3.[24,37,38] The Pt catalyst plays a primary role in the intercalation process, as without it the resistance of WO_3 remains constant upon exposure to H_2 (Figure S1). Increasing (decreasing) the amount of Pt catalyst, the material response to hydrogen can be made faster (slower), as discussed in Figure S2. In our experiments, the hydrogen is diluted in a carrier gas. We tested different inert gases (Ar, N_2, and He) and observed similar responses, indicating they have a negligible contribution in the intercalation process (Figure S3). While still showing a good response, a slower intercalation rate is observed when the carrier gas is air. We attribute this difference to the presence of O_2 molecules that can react with H atoms to form water.[36] The intercalation rate is also reduced when no carrier gas is used, even if the H_2 partial pressure is the same. The rate of the deintercalation process is quite slow both in a vacuum and in an inert gas atmosphere, while it is significantly enhanced in the presence of O_2 molecules (further details in Figure S4).

Hydrogen Sensing. The strong and fast response of single-crystal WO_3 ultrathin films to H_2 makes them appealing candidates to develop hydrogen gas sensors. For this purpose, we characterize in Figure 3a the resistive changes of WO_3 for different values of C_{H_2}. The measurements are performed with the following experimental procedure: (i) evacuation of the sample chamber ($p < 1 \times 10^{-4}$ mbar), (ii) exposure to the H_2/Ar mixture at 1 bar total pressure for 1 min, (iii) chamber evacuation, and (iv) exposure to air at 1 bar for 10 min. This procedure is repeated for different hydrogen concentrations between 1 and 4000 ppm and for two sample temperatures, namely 25 and 65 °C. We note that steps (i) and (iii) are used to remove H_2 and O_2 from the gas chambers, respectively, thus guaranteeing high purity of the mixtures used in the subsequent steps (ii) and (iv). The resistance drop ΔR during step (ii) becomes progressively larger with increasing C_{H_2}, and it is almost independent of C_{H_2} at high hydrogen concentration, indicating a saturation regime. In the vacuum step (iii), a small increase of resistance is observed, and it is more pronounced at 65 °C. Upon exposure to air in step (iv), the resistance recovers toward the initial value. We note that due to the short duration of this step, the resistance recovery at the highest values of C_{H_2} is not complete. However, as discussed below, this does not influence the sensor operation. Raising the temperature determines a faster response and higher sensitivity, with an overall similar sample behavior.

We can quantitatively evaluate the performance of WO_3 as an H_2 sensor by considering the relative resistance change $\Delta R/$

DOI: 10.1021/acsanm.8b00627
ACS Appl. Nano Mater. 2018, 1, 3446−3452

R_0 at 1 s after the introduction of H_2 gas. This analysis is reported in Figure 3b, where we show that at intermediate concentrations (solid markers) the response depends on C_{H_2} according to the power law $\Delta R/R_0 \sim (C_{H_2})^{\alpha}$. We find $\alpha = 1.3$ at 25 °C and $\alpha = 1.5$ at 65 °C, indicating that a similar relationship regulates the trend at both temperatures. The onset of the saturated response of the WO3 device (shaded markers in Figure 3b) depends on its operational temperature. At 25 °C the response follows the power law in the range 10−1000 ppm, while at 65 °C this window is shifted to lower concentrations in the range 1−100 ppm. This indicates that by increasing the sensor temperature by a few tens of degrees, it is possible to lower the detection limit by 1 order of magnitude or, in other words, that the sensitivity range can be tuned by controlling the sample temperature.

To evaluate the response time of WO_3, we consider a simplified model describing the time-dependent resistance change as $\Delta R/R_0 \sim e^{-t/\tau}$, where the response time τ is the fitting parameter. We find a lower τ for higher hydrogen concentration and sample temperature in step (ii), reaching $\tau = 1$ s for $C_{H_2} = 100$ ppm at 65 °C (Figure 3c). We note that independently of the value of τ and in the whole range of explored parameters, the presence of hydrogen is always detectable within the 1 min time frame used in the experiments. Figure 3d shows the recovery time of doped WO_3 after exposing the device to air in step (iv). Again, lower τ is measured at higher temperature and higher initial hydrogen concentration in WO_3. Finally, we note that the sensor response is independent of the initial resistance value R_0 (Figure S5), meaning that in the explored range of parameters WO_3 works as a differential sensor, with a response depending only on C_{H_2} and not on the doping state of the material. In addition, the sensor preserves its functionality in a low-pressure H_2 atmosphere, demonstrating its operability also as possible detector for pure H_2 gas (Figure S6). These characteristics make WO_3 an interesting material for H_2 sensing that can be used in a large variety of environments.

Kinetic Model. To obtain an insight into the mechanism regulating the doping of WO_3 thin films, we study the intercalation and deintercalation kinetics in a controlled atmosphere. For this purpose, we consider the minimal model of two-step reactions schematically illustrated in Figure 4a, where each step is described by a rate constant k_a, and its reverse by k_{-a}. We describe the intercalation and deintercalation processes by the balance equations

$$H_2 \xrightarrow{k_{1,i}} 2H_{(Pt)} \underset{k_{-2,i}}{\overset{k_{2,i}}{\rightleftharpoons}} 2H_{(bulk)} \tag{1a}$$

$$2H_{(bulk)} \underset{k_{2,d}}{\overset{k_{-2,d}}{\rightleftharpoons}} 2H_{(surf.)} \xrightarrow{k_{-1,d}} H_2 \tag{1b}$$

where with $H_{(Pt)}$ we indicate a hydrogen atom on a catalyst site, with $H_{(surf.)}$ anywhere on WO_3 or Pt surface, and with $H_{(bulk)}$ intercalated in the WO_3 lattice. Our model describes the intercalation and deintercalation considering different initial conditions. The intercalation experiment starts with undoped WO_3 and an infinite reservoir of H_2 in gas phase, allowing to consider the dissociative adsorption ($k_{1,i}$) of H_2 on Pt as an irreversible process. The subsequent hydrogen exchange between WO_3 surface and WO_3 bulk is an equilibrium reaction, regulated by rate constants $k_{2,i}$ and $k_{-2,i}$. The

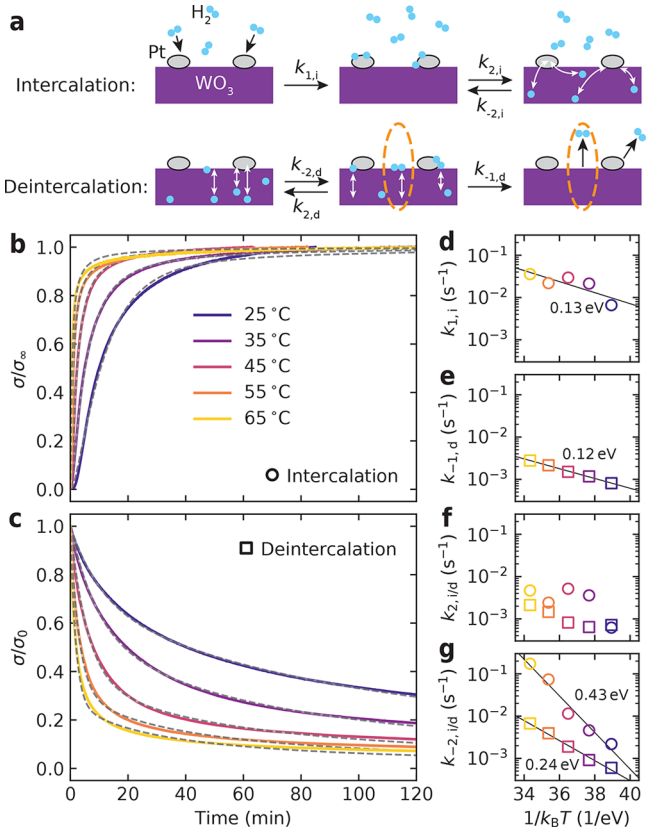

Figure 4. Kinetics of hydrogen intercalation and deintercalation. (a) Schematics of the processes involved in H_2 exchange with WO_3. The rate constants associated with each process are indicated on the respective reaction arrow. (b) Experimental curves of intercalation in low-pressure hydrogen mixture (C_{H_2} = 20%, 5 mbar total pressure). (c) Deintercalation curves (vacuum atmosphere) at different temperatures. The conductance is divided by its final (σ_∞) and initial (σ_0) value for intercalation and deintercalation curves, respectively. The dashed lines are fits obtained from numerical solution of eqs 1a and 1b. (d−g) Rate constants extracted from the fits. The solid lines are Arrhenius fits used to extract the activation energy of the reaction steps.

deintercalation experiment is modeled considering an initial condition where WO_3 is in a state of saturated doping and in a vacuum atmosphere. Hydrogen atoms in the crystal lattice migrate toward and from the surface (rate constants $k_{-2,d}$ and $k_{2,d}$) where they can recombine to form H_2. Differently from the intercalation process, in this step the hydrogen recombines in a spontaneous reaction that does not require a catalyst. H_2 molecules can thus form anywhere on WO_3 surface. Subsequently, hydrogen molecules desorb and are pumped away in an irreversible process ($k_{-1,d}$).

Hydrogen intercalation is experimentally studied starting from an undoped, low-conductance state. In Figure 4b we show intercalation curves performed in a low-pressure (5 mbar) gas mixture with C_{H_2} = 20% at different sample temperatures. Higher temperatures determine faster intercalation, with the conductance reaching a saturation value after a few tens of minutes. The deintercalation process in Figure 4c is studied starting with WO_3 in a high-conductance state. At the beginning of the measurement, WO_3 is exposed to a vacuum atmosphere, and the conductance decreases over time, with a faster rate at higher temperature. We note that in vacuum the

DOI: 10.1021/acsanm.8b00627
ACS Appl. Nano Mater. 2018, 1, 3446−3452

deintercalation process is much slower than in air, so that the curves do not reach full saturation in the duration of the experiment (2 h), in agreement with our interpretation of the role played by oxygen in accelerating the desorption process (Figure S4).

The kinetic equations associated with the reactions in eqs 1a and 1b (see also the Supporting Information) are solved numerically to fit the experimental data (dashed lines in Figures 4b and 4c). Our model shows good agreement with the measurements and allows us to extract the rate constants of the different processes (Figures 4d to 4g). We find that $k_{1,i}$ is at all temperatures 1 order of magnitude larger than $k_{-1,d}$, signaling a faster rate of H_2 splitting compared to its recombination. This difference supports our choice to consider the dissociative adsorption of H_2 an irreversible process during the intercalation experiment (i.e., $k_{-1,i} \ll k_{1,i}$). In the deintercalation experiment, instead, $k_{-1,d}$ becomes important because the vacuum atmosphere hinders the H_2 splitting reaction by carrying away the H_2 molecules as soon as they form. We fit the temperature dependence of the rate constants with an Arrhenius model, finding activation energies of 0.13 eV for $k_{1,i}$ and 0.12 eV for $k_{-1,d}$. These results can be compared with *ab initio* computations that find activation energies in the range 0.06−0.42 eV for the dissociative chemisorption on Pt surfaces, with lower values expected for smaller particles.[39,40] Similarly, recombinative desorption at oxide surfaces entails activation energies in the range 0.05−0.9 eV depending on the hydrogen binding energy at the adsorption site.[41]

The surface-to-bulk diffusion rate constants $k_{2,i/d}$ show a weak temperature dependence (Figure 4f). The bulk-to-surface rates $k_{-2,i/d}$ in Figure 4g, instead, show a linear trend which allows to extract activation energies of 0.43 and 0.24 eV in the intercalation and deintercalation experiments, respectively. The higher activation energy required during intercalation stems from the fact that hydrogen splitting can only happen on the catalyst particles, so that the hydrogen atoms have to overcome two energy barriers: the diffusion on WO_3 surface and then the diffusion in WO_3 bulk. During deintercalation, instead, $k_{-2,d}$ is only related to the hydrogen diffusion in WO_3 bulk because recombination can happen anywhere on the WO_3 surface. Previous experimental and density functional theory calculations reported energy barriers between 0.26 and 0.37 eV for hydrogen migration from the Pt sites to WO_3 surface,[42,43] which are compatible with our experimental results.

Electrical Transport. The previous analysis showed that both intercalation and deintercalation are thermally activated processes, so that their rate can be controlled changing the sample temperature. Furthermore, we showed that the room temperature resistivity of WO_3 films can be continuously tuned by H_2 intercalation. As a result, hydrogen kinetics in the WO_3 lattice can be arrested by cooling down the material. This allows to get an insight into the electronic doping mechanism by measuring the transport activation energy of the free carriers induced by hydrogen doping. In Figure 5a, we show a series of resistance versus temperature curves measured on a single WO_3 device under different doping conditions. Before each measurement, we expose the sample to hydrogen gas at room temperature in order to obtain the desired sheet resistance $\rho_{300\,K}$, after which we evacuate the sample chamber and start a cooling ramp. All curves show a semiconducting trend, where higher doping produces a shallower temperature dependence. We note that the resistance versus temperature curves are similar to what previously reported for WO_3 doped

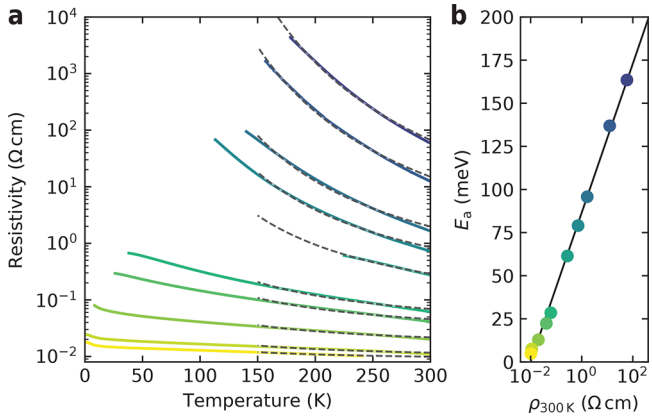

Figure 5. Low-temperature transport at different levels of H_2 doping. (a) Resistance versus temperature curves of a single WO_3 device. The dashed lines are fits with the Arrhenius model for activated transport. (b) Activation energy as a function of room temperature resistivity $\rho_{300\,K}$. The solid line is a linear regression to the data points.

with oxygen vacancies,[31,44] suggesting the occurrence of a similar mechanism of extrinsic doping. This interpretation is supported by recent experiments on WO_3 nanowires which showed that H_2 intercalation is accompanied by the formation of interstitial H_2O molecules along with oxygen vacancies.[36,45]

We consider an Arrhenius mechanism to describe the temperature dependence of the electrical transport $\sigma = 1/\rho \sim e^{-E_a/k_BT}$, where E_a is the activation energy. The resulting fits in the high-temperature regime (above 150 K, dashed lines) show good agreement with the experimental data and allow to extract the trend of E_a as a function of $\rho_{300\,K}$ reported in Figure 5b. The data show the logarithmic dependence $E_a = A \log \rho_{300\,K} + B$, with $A = 19$ meV and $B = 90$ meV. We show in the Supporting Information that the activation energy can be expressed as

$$E_a = k_B T_{300\,K}[\log \rho_{300\,K} + \gamma \log C_H] + \gamma T_{300\,K} \Delta S^\circ \qquad (2)$$

where γ is related to the extrinsic donor charge, ΔS° is the reaction entropy, and C_H is the hydrogen concentration inside the WO_3 lattice. Equation 2 provides a direct relation between E_a and $\rho_{300\,K}$ through the coefficient $k_B T_{300\,K} \sim 26$ meV. However, $\rho_{300\,K}$ is also a function of C_H, and by comparing eq 2 with the experimental fit, we find that the resistivity can be expressed as $\rho_{300\,K} \sim (C_H)^{-\gamma/0.3}$. We show in the Supporting Information that $\gamma = 1/3$ if the electron donors are oxygen vacancies. Substituting this value, we obtain an almost linear relationship between the conductance and hydrogen concentration in the material $\sigma_{300\,K} = 1/\rho_{300\,K} \sim C_H$, in agreement with the assumption we used to treat the experimental intercalation and deintercalation curves with the kinetic model. The linear dependence between hydrogen concentration in WO_3 and electrical conductivity constitutes a powerful transduction scheme for the electrical sensing of H_2 gas.

CONCLUSIONS

To conclude, single-crystal Pt-decorated WO_3 ultrathin films have proven extremely sensitive and fast probes for solid state hydrogen gas sensors. Thanks to the high crystal quality and high surface-to-volume ratio, our devices showed a 5 orders of magnitude change in electrical resistivity upon exposure to H_2 gas at room temperature. The device response can be tuned by

DOI: 10.1021/acsanm.8b00627
ACS Appl. Nano Mater. 2018, 1, 3446−3452

controlling the temperature, enabling detection of a hydrogen concentration down to 10 ppm at room temperature and down to 1 ppm at 65 °C, where we measured short response times as low as 1 s for concentrations above 100 ppm. We successfully modeled the intercalation and deintercalation of hydrogen in the WO_3 lattice with a kinetic of thermally activated processes. Our analysis allowed to extract the activation energies of the different reactions, which are in good agreement with previous reports based on *ab initio* calculations. These results show that heteroepitaxial WO_3 films hold great potential for high-performance hydrogen gas sensors, providing high sensitivity, fast response, high dynamic range, and a simple device architecture.

EXPERIMENTAL SECTION

Sample Growth. WO_3 thin films were grown by pulsed laser deposition on commercially available 5 mm × 5 mm $SrTiO_3$ (001) substrates, with TiO_2 surface termination. The laser ablation was performed using a KrF excimer laser (Coherent COMPexPro 205, λ = 248 nm) with a 1 Hz repetition rate and 1 J cm^{-2} fluence. The target-to-substrate distance was fixed at 55 mm. The WO_3 films were deposited from a WO_3 sintered target at 500 °C substrate temperature and 8 × 10^{-2} mbar oxygen pressure. Film thickness was monitored *in situ* during growth by intensity oscillations of reflection high-energy electron diffraction (RHEED). At the end of the growth, the films were cooled down to room temperature in the same oxygen pressure used during deposition. Further details on the growth and sample characterization are reported in ref 31.

Van Der Pauw Geometry Fabrication. Standard e-beam lithography with PMMA resist was used to pattern WO_3 heteroepitaxial films. The metal contacts were deposited by evaporation of 5 nm Ti and 45 nm Au at room temperature, followed by lift-off. Ar ion etching was used prior to metal deposition to etch 5 nm of WO_3 in order to provide edge contacts to the film in an interdigitated pattern, which ensure a low contact resistance. The WO_3 mesa was defined by a subsequent lithographical and etching step which fully removes the WO_3 material from the regions surrounding the van der Pauw geometry. The etching was performed using a beam current of 2 mA and an energy of 500 eV, corresponding to an Ar ion flux of 0.25 mA cm^{-2}. These parameters produce etched regions which are insulating at all temperatures.

Gas Mixture Preparation. To regulate the H_2 concentration with high precision, we used the series of vacuum chambers described in Figure 1f: the preparation chambers PC1, PC2, and sample chamber SC1 having volume ratios 1:9:1. Before introduction of the gases, the chambers were evacuated to p < 0.1 μ bar. The hydrogen gas was sourced from a bottle of 20% H_2/Ar. This gas blend was first introduced and measured by a pressure sensor in PC1 and then expanded to the volume PC1 + PC2, where pure Ar gas was introduced in order to reach the desired total pressure. To begin the experiment, the gas mixture was finally allowed to enter SC1. For example, to achieve the lowest hydrogen concentration used in the experiment (1 ppm in 1 bar total pressure), PC1 is first filled up with 55 μbar of H_2 blend. We note that this value can be precisely evaluated as it is well above both the lower detection limit (1 μbar) of the pressure sensor used for the measurement and the chamber base pressure (0.1 μbar). The gas mixture is then introduced in the volume PC1 + PC2, where it is topped up with Ar to reach the total pressure of 1.1 bar. Finally, the sample is exposed to the gas mixture at 1 bar in the total volume PC1 + PC2 + SC1.

Electrical Measurements. The resistive measurements were performed with a Keithley 6430 sourcemeter using a four-probe configuration and a current bias of 100 nA.

Air Conditions. Air from the environment (relative humidity 50%) was used in the sensing measurements.

Numerical Solution of Kinetic Equations. The kinetic model in the Supporting Information was solved using the NDSolve function of Wolfram Mathematica. The resulting fit curves yield a coefficient R^2 ~ 0.99, indicating that our model is a good approximation of the experimental reactions, although higher-order corrections might be present.

ASSOCIATED CONTENT

Supporting Information

The Supporting Information is available free of charge on the ACS Publications website at DOI: 10.1021/acsanm.8b00627.

Characterization of the Pt catalyst role, effect of different carrier gases on hydrogen intercalation and deintercalation, sensing properties with different sensor initial resistance, sensing in a low-pressure H_2 mixture, kinetic models for intercalation and deintercalation, model for activated electrical transport (PDF)

Video of WO_3 color change (AVI)

AUTHOR INFORMATION

Corresponding Author

*E-mail: g.mattoni@tudelft.nl (G.M.).

ORCID

Giordano Mattoni: 0000-0002-3678-9168

Nicola Manca: 0000-0002-7768-2500

Notes

The authors declare no competing financial interest.

ACKNOWLEDGMENTS

The authors thank D. Davidovikj, P.G. Steeneken, T. van der Sar, M. Scarselli, L. Pellegrino, and A. Gerbi for fruitful discussions and important suggestions. This work was supported by The Netherlands Organisation for Scientific Research (NWO/OCW) as part of the Frontiers of Nanoscience program (NanoFront) and by the Dutch Foundation for Fundamental Research on Matter (FOM). The research leading to these results has received funding from the European Research Council under the European Union's H2020 programme/ERC Grant Agreement no. 677458.

REFERENCES

(1) Zubko, P.; Gariglio, S.; Gabay, M.; Ghosez, P.; Triscone, J.-M. Interface Physics in Complex Oxide Heterostructures. *Annu. Rev. Condens. Matter Phys.* **2011**, *2*, 141−165.

(2) Ahn, C. H.; Triscone, J.-M.; Mannhart, J. Electric Field Effect in Correlated Oxide Systems. *Nature* **2003**, *424*, 1015−1018.

(3) Caviglia, A.; Gariglio, S.; Reyren, N.; Jaccard, D.; Schneider, T.; Gabay, M.; Thiel, S.; Hammerl, G.; Mannhart, J.; Triscone, J.-M. Electric Field Control of the $LaAlO_3/SrTiO_3$ Interface Ground State. *Nature* **2008**, *456*, 624−627.

(4) Kalinin, S. V.; Spaldin, N. A. Functional Ion Defects in Transition Metal Oxides. *Science* **2013**, *341*, 858−859.

(5) Muller, D. A.; Nakagawa, N.; Ohtomo, A.; Grazul, J. L.; Hwang, H. Y. Atomic-scale Imaging of Nanoengineered Oxygen Vacancy Profiles in $SrTiO_3$. *Nature* **2004**, *430*, 657−661.

(6) Jeong, J.; Aetukuri, N.; Graf, T.; Schladt, T. D.; Samant, M. G.; Parkin, S. S. P. Suppression of Metal-Insulator Transition in VO_2 by Electric Field-Induced Oxygen Vacancy Formation. *Science* **2013**, *339*, 1402−1405.

(7) Mattoni, G.; Baek, D. J.; Manca, N.; Verhagen, N.; Groenendijk, D.; Kourkoutis, L. F.; Filippetti, A.; Caviglia, A. D. Insulator-to-Metal Transition at Oxide Interfaces Induced by WO_3 Overlayers. *ACS Appl. Mater. Interfaces* **2017**, *9*, 42336.

(8) Stambouli, A. B.; Traversa, E. Solid Oxide Fuel Cells (SOFCs): A Review of an Environmentally Clean and Efficient Source of Energy. *Renewable Sustainable Energy Rev.* **2002**, *6*, 433−455.

DOI: 10.1021/acsanm.8b00627
ACS Appl. Nano Mater. 2018, 1, 3446−3452

(9) Kharton, V. V.; Marques, F. M. B.; Atkinson, A. Transport Properties of Solid Oxide Electrolyte Ceramics: A Brief Review. *Solid State Ionics* **2004**, *174*, 135−149.
(10) Waser, R.; Aono, M. Nanoionics-Based Resistive Switching Memories. *Nat. Mater.* **2007**, *6*, 833−840.
(11) Ha, S. D.; Ramanathan, S. Adaptive Oxide Electronics: A Review. *J. Appl. Phys.* **2011**, *110*, 071101.
(12) Manca, N.; Pellegrino, L.; Marré, D. Reversible Oxygen Vacancies Doping in $(La_{0.7},Sr_{0.3})MnO_3$ Microbridges by Combined Self-heating and Electromigration. *Appl. Phys. Lett.* **2015**, *106*, 203502.
(13) Prezioso, M.; Merrikh-Bayat, F.; Hoskins, B. D.; Adam, G. C.; Likharev, K. K.; Strukov, D. B. Training and Operation of an Integrated Neuromorphic Network Based on Metal-oxide Memristors. *Nature* **2015**, *521*, 61−64.
(14) Kumar, S.; Strachan, J. P.; Williams, R. S. Chaotic Dynamics in Nanoscale NbO_2 Mott Memristors for Analogue Computing. *Nature* **2017**, *548*, 318−321.
(15) Swallow, J. G.; Kim, J. J.; Maloney, J. M.; Chen, D.; Smith, J. F.; Bishop, S. R.; Tuller, H. L.; Van Vliet, K. J. Dynamic Chemical Expansion of Thin-film Non-stoichiometric Oxides at Extreme Temperatures. *Nat. Mater.* **2017**, *16*, 749−754.
(16) Zhang, J.; Liu, X.; Neri, G.; Pinna, N. Nanostructured Materials for Room-Temperature Gas Sensors. *Adv. Mater.* **2016**, *28*, 795−831.
(17) Hübert, T.; Boon-Brett, L.; Black, G.; Banach, U. Hydrogen Sensors-A Review. *Sens. Actuators, B* **2011**, *157*, 329−352.
(18) Phanichphant, S. Semiconductor Metal Oxides as Hydrogen Gas Sensors. *Procedia Eng.* **2014**, *87*, 795−802.
(19) Varghese, O. K.; Gong, D.; Paulose, M.; Ong, K. G.; Grimes, C. A. Hydrogen Sensing Using Titania Nanotubes. *Sens. Actuators, B* **2003**, *93*, 338−344.
(20) Wang, B.; Zhu, L. F.; Yang, Y. H.; Xu, N. S.; Yang, G. W. Fabrication of a SnO_2 Nanowire Gas Sensor and Sensor Performance for Hydrogen. *J. Phys. Chem. C* **2008**, *112*, 6643−6647.
(21) Strelcov, E.; Lilach, Y.; Kolmakov, A. Gas Sensor Based on Metal-Insulator Transition in VO_2 Nanowire Thermistor. *Nano Lett.* **2009**, *9*, 2322−2326.
(22) Long, H.; Zeng, W.; Zhang, H. Synthesis of WO_3 and its Gas Sensing: A Review. *J. Mater. Sci.: Mater. Electron.* **2015**, *26*, 4698−4707.
(23) Granqvist, C. G. Electrochromic Tungsten Oxide Films: Review of Progress 1993−1998. *Sol. Energy Mater. Sol. Cells* **2000**, *60*, 201−262.
(24) Wang, M.; Shen, S.; Ni, J.; Lu, N.; Li, Z.; Li, H.-B.; Yang, S.; Chen, T.; Guo, J.; Wang, Y.; Xiang, H.; Yu, P. Electric-Field-Controlled Phase Transformation in WO_3 Thin Films through Hydrogen Evolution. *Adv. Mater.* **2017**, *29*, 1703628.
(25) Ippolito, S. J.; Kandasamy, S.; Kalantar-Zadeh, K.; Wlodarski, W. Hydrogen Sensing Characteristics of WO_3 Thin Film Conductometric Sensors Activated by Pt and Au Catalysts. *Sens. Actuators, B* **2005**, *108*, 154−158.
(26) Hsu, W.-C.; Chan, C.-C.; Peng, C.-H.; Chang, C.-C. Hydrogen Sensing Characteristics of an Electrodeposited WO_3 Thin Film Gasochromic Sensor Activated by Pt Catalyst. *Thin Solid Films* **2007**, *516*, 407−411.
(27) Calavia, R.; Mozalev, A.; Vazquez, R.; Gracia, I.; Cané, C.; Ionescu, R.; Llobet, E. Fabrication of WO_3 Nanodot-Based Microsensors Highly Sensitive to Hydrogen. *Sens. Actuators, B* **2010**, *149*, 352−361.
(28) Kukkola, J.; Mohl, M.; Leino, A.-R.; Mäklin, J.; Halonen, N.; Shchukarev, A.; Konya, Z.; Jantunen, H.; Kordas, K. Room Temperature Hydrogen Sensors Based on Metal Decorated WO_3 Nanowires. *Sens. Actuators, B* **2013**, *186*, 90−95.
(29) Boudiba, A.; Zhang, C.; Umek, P.; Bittencourt, C.; Snyders, R.; Olivier, M.-G.; Debliquy, M. Sensitive and Rapid Hydrogen Sensors Based on Pd-WO_3 Thick Films with Different Morphologies. *Int. J. Hydrogen Energy* **2013**, *38*, 2565−2577.
(30) Liu, B.; Cai, D.; Liu, Y.; Wang, D.; Wang, L.; Wang, Y.; Li, H.; Li, Q.; Wang, T. Improved Room-temperature Hydrogen Sensing Performance of Directly Formed Pd/WO_3 Nanocomposite. *Sens. Actuators, B* **2014**, *193*, 28−34.
(31) Mattoni, G.; Filippetti, A.; Manca, N.; Zubko, P.; Caviglia, A. D. Charge Doping and Large Lattice Expansion in Oxygen-Deficient Heteroepitaxial WO_3. *Phys. Rev. Mater.* **2018**, *2*, 053402.
(32) Sermon, P. A.; Bond, G. C. Hydrogen Spillover. *Catal. Rev.: Sci. Eng.* **1974**, *8*, 211−239.
(33) Yoon, H.; Choi, M.; Lim, T.-W.; Kwon, H.; Ihm, K.; Kim, J. K.; Choi, S.-Y.; Son, J. Reversible Phase Modulation and Hydrogen Storage in Multivalent VO_2 Epitaxial Thin Films. *Nat. Mater.* **2016**, *15*, 1113−1119.
(34) Crandall, R. S.; Faughnan, B. W. Dynamics of Coloration of Amorphous Electrochromic Films of WO_3 at Low Voltages. *Appl. Phys. Lett.* **1976**, *28*, 95−97.
(35) Chen, H.; Xu, N.; Deng, S.; Lu, D.; Li, Z.; Zhou, J.; Chen, J. Gasochromic Effect and Relative Mechanism of WO_3 Nanowire Films. *Nanotechnology* **2007**, *18*, 205701.
(36) Zhu, L. F.; She, J. C.; Luo, J. Y.; Deng, S. Z.; Chen, J.; Xu, N. S. Study of Physical and Chemical Processes of H_2 Sensing of Pt-coated WO_3 Nanowire Films. *J. Phys. Chem. C* **2010**, *114*, 15504−15509.
(37) Shaver, P. J. Activated Tungsten Oxide Gas Detectors. *Appl. Phys. Lett.* **1967**, *11*, 255−257.
(38) Kılıc, C.; Zunger, A. n-type Doping of Oxides by Hydrogen. *Appl. Phys. Lett.* **2002**, *81*, 73−75.
(39) Campbell, C. T. Ultrathin Metal Films and Particles on Oxide Surfaces: Structural, Electronic and Chemisorptive Properties. *Surf. Sci. Rep.* **1997**, *27*, 1−111.
(40) Zhou, C.; Wu, J.; Nie, A.; Forrey, R. C.; Tachibana, A.; Cheng, H. On the Sequential Hydrogen Dissociative Chemisorption on Small Platinum Clusters: A Density Functional Theory Study. *J. Phys. Chem. C* **2007**, *111*, 12773−12778.
(41) Mackay, K. K.; Freund, J. B.; Johnson, H. T. Hydrogen Recombination Rates on Silica from Atomic-Scale Calculations. *J. Phys. Chem. C* **2016**, *120*, 24137−24147.
(42) Triwahyono, S.; Yamada, T.; Hattori, H. Kinetic Study of Hydrogen Adsorption on Pt/WO_3-ZrO_2 and WO_3-ZrO_2. *Appl. Catal., A* **2003**, *250*, 65−73.
(43) Xi, Y.; Zhang, Q.; Cheng, H. Mechanism of Hydrogen Spillover on WO_3 (001) and Formation of H_xWO_3 (x = 0.125, 0.25, 0.375, and 0.5). *J. Phys. Chem. C* **2014**, *118*, 494−501.
(44) Altendorf, S. G.; Jeong, J.; Passarello, D.; Aetukuri, N. B.; Samant, M. G.; Parkin, S. S. P. Facet-Independent Electric-field-Induced Volume Metallization of Tungsten Trioxide Films. *Adv. Mater.* **2016**, *28*, 5284−5292.
(45) Luo, J. Y.; Deng, S. Z.; Tao, Y. T.; Zhao, F. L.; Zhu, L. F.; Gong, L.; Chen, J.; Xu, N. S. Evidence of Localized Water Molecules and Their Role in the Gasochromic Effect of WO_3 Nanowire Films. *J. Phys. Chem. C* **2009**, *113*, 15877−15881.

DOI: 10.1021/acsanm.8b00627
ACS Appl. Nano Mater. 2018, 1, 3446−3452